The Astrophysical Journal, 994:247 (16pp), 2025 December 1 https://doi.org/10.3847/1538-4357/ae1013

Multiphase Gas Offsets in the Atmospheres of Central Galaxies and Their Consequences for SMBH Activation. I. The Hot and Warm Ionized Gas Phases

Francesco Ubertosi[1,2], Fabrizio Brighenti[1,3], Ewan O'Sullivan[4], Gerrit Schellenberger[4], Myriam Gitti[1,2], Simona Giacintucci[5], Pasquale Temi[6], Laurence P. David[4], Jan Vrtilek[4], Tiziana Venturi[2], Elisabetta Liuzzo[2], Marcella Massardi[2], and Kamlesh Rajpurohit[4]
[1] Dipartimento di Fisica e Astronomia, Università di Bologna, via Gobetti 93/2, I-40129 Bologna, Italy; francesco.ubertosi2@unibo.it
[2] Istituto Nazionale di Astrofisica—Istituto di Radioastronomia (IRA), via Gobetti 101, I-40129 Bologna, Italy
[3] University of California Observatories/Lick Observatory, Department of Astronomy and Astrophysics, Santa Cruz, CA 95064, USA
[4] Center for Astrophysics | Harvard & Smithsonian, 60 Garden Street, Cambridge, MA 02138, USA
[5] Naval Research Laboratory, 4555 Overlook Avenue SW, Code 7213, Washington, DC 20375, USA
[6] NASA Ames Research Center, MS 245-6, Moffett Field, CA 94035-1000, USA
Received 2025 August 12; revised 2025 September 26; accepted 2025 October 3; published 2025 November 28

Abstract

We investigate the spatial relationships between multiphase gas components and supermassive black hole (SMBH) activity in a sample of 25 cool-core galaxy groups and clusters. Using high-angular-resolution observations from Chandra, the Very Large Telescope/Multi Unit Spectroscopic Explorer, and the Very Long Baseline Array (VLBA), we robustly locate the positions, respectively, of the X-ray peak of the intracluster medium, of the Hα peak of the warm ionized gas, and of the SMBH radio core, on parsec scales. We identify spatial offsets between the X-ray peak of the hot gas and the SMBH in 80% of the systems, with an average displacement of $\langle\Delta^{\rm SMBH}_{\rm X\text{-}ray}\rangle = 4.8$ kpc (dispersion of 3.8 kpc). In contrast, the peak of warm ionized gas traced by Hα exhibits a much smaller offset ($\langle\Delta^{\rm SMBH}_{\rm H\alpha}\rangle = 0.6$ kpc; dispersion of 1.4 kpc) and a lower incidence of displacement (15%). Our findings suggest that hot-gas sloshing primarily drives the observed spatial offsets, with active galactic nucleus (AGN)–driven uplift contributing in some systems. Importantly, systems with Hα–SMBH offsets of $\geqslant$1 kpc uniformly lack detectable radio cores on VLBA scales, with upper limits on the 5 GHz power of $P_{\rm 5GHz} \leqslant 10^{21-22}$ W Hz^{-1}, while those without such offsets exhibit radio-powerful AGNs with parsec-scale radio emission up to $P_{\rm 5GHz} \sim 10^{24-25}$ W Hz^{-1}. This correlation indicates that centrally concentrated warm gas is critical for sustaining radio-loud SMBH activity, possibly supporting scenarios of cold-mode accretion. Overall, our results highlight the importance of high-angular-resolution multiwavelength observations for understanding the interplay between multiphase gas cooling and AGN fueling in central galaxies.

Unified Astronomy Thesaurus concepts: Supermassive black holes (1663); Accretion (14); Galaxy clusters (584); Galaxy groups (597); Cooling flows (2028); Galaxy evolution (594); X-ray astronomy (1810); Intracluster medium (858); Interstellar medium (847)

1. Introduction

A key component of the baryon cycle in galaxy groups and clusters is the gaseous halo of these systems. The so-called intracluster or intragroup medium (ICM/IGrM) can lose energy by thermally radiating in the X-ray band, potentially leading to the condensation of the hot gas into cooler phases. In turn, these phases can support star formation at the center of the system, the cool core (e.g., for reviews, see W. G. Mathews & F. Brighenti 2003; M. Donahue & G. M. Voit 2004, 2022). This process does not proceed undisturbed: the brightest cluster/group galaxy (BCG/BGG) typically hosts a supermassive black hole (SMBH) that, when active, drives powerful jets through the surrounding medium, thereby depositing energy and reducing the efficiency of the cooling process (e.g., for reviews, see B. R. McNamara & P. E. J. Nulsen 2007, 2012; A. C. Fabian 2012; M. Gitti et al. 2012; M. Gaspari et al. 2020; D. Eckert et al. 2021). This active galactic nucleus (AGN) feedback mechanism is vital for explaining the long-term evolution of inflow and outflow processes in groups and clusters.

In virialized, perfectly relaxed galaxy groups and clusters, the BCG/BGG is expected to reside at the center of the potential well of its host cluster, coinciding with the peaks of the hot ICM, of the warm ionized gas, and of the cold molecular phase (e.g., F. C. van den Bosch et al. 2005; W. Cui et al. 2016). Indeed, numerous studies have demonstrated that the hot, warm, and molecular gas phases are interconnected over long timescales, as evidenced by, for example, correlations between the hot-gas surface brightness, entropy, or cooling time and Hα luminosity (e.g., K. W. Cavagnolo et al. 2009; A. J. R. Sanderson et al. 2009), spatial alignment between the warm and molecular gas phases with the X-ray cooling region (e.g., M. McDonald et al. 2010; V. Olivares et al. 2019, 2025; H. R. Russell et al. 2019), and relations linking the molecular gas mass to X-ray gas mass and Hα emission (A. C. Edge 2001; F. A. Pulido et al. 2018; V. Olivares et al. 2022).

However, in some cases, the X-ray and Hα emission peaks tracing gas cooling are separated from the BCG core (S. L. Hamer et al. 2012; T. Pasini et al. 2021; L. Rosignoli et al. 2024). For example, in a sample of 65 X-ray-selected clusters, A. J. R. Sanderson et al. (2009) found that all of the

BCGs/BGGs with warm-gas detections (i.e., in cool-core systems) are separated from the X-ray peak by less than about 15 kpc (see also D. S. Hudson et al. 2010). The origins of the observed offsets are generally attributed to gravitational disturbances in the cluster potential, often triggered by minor mergers that induce sloshing motions of the gas. Sloshing consists of the gas peak being offset from the bottom of the potential well and subsequently falling back (e.g., Y. Ascasibar & M. Markevitch 2006; M. Markevitch & A. Vikhlinin 2007; J. A. Zuhone & E. Roediger 2016). Ram pressure slows the motion of the gas, thus creating a temporary offset between the galaxy and its gaseous halo, as well as offsets among the different gas phases (e.g., E. T. Million et al. 2010; S. L. Hamer et al. 2012). Another plausible mechanism for displacing the ICM/IGrM from the BCG/BGG is mechanical uplift by AGN jets, which can distort the otherwise centrally concentrated configuration of the cool core (e.g., C. C. Kirkpatrick & B. R. McNamara 2015; B. R. McNamara et al. 2016). While AGN-driven outflows are capable of lifting portions of the X-ray-emitting gas (e.g., N. Werner et al. 2010; M. Gitti et al. 2011), existing studies suggest that jets are not capable of removing the entire dense, cool gas reservoir from the galaxy (L. Rosignoli et al. 2024).

Past studies have explored the consequences of these spatial offsets on ICM/IGrM cooling and on AGN feedback. The results indicate that clusters with a larger BCG–X-ray peak separation have a weaker cool core (A. J. R. Sanderson et al. 2009); that cooling (traced by the detection of molecular gas) persists in hot- and warm-gas peaks even when these are offset from the BCG (S. L. Hamer et al. 2012); and that over long timescales, AGN feedback remains effective despite the temporary displacement of the gaseous atmosphere (T. Pasini et al. 2021; L. Rosignoli et al. 2024).

However, the consequences of these spatial offsets on AGN feeding (i.e., the process through which gas sinks at the center of the galaxy and fuels the SMBH activity) remain mostly unexplored. A key implication of a multiphase AGN feeding scenario is that if a particular gas phase directly fuels the AGN, then a sustained spatial offset between this gas phase and the BCG should correspond to a quiescent SMBH. We have thus started a project to explore multiphase gas offsets in central galaxies and their connection to the SMBH activation. In this first work (Paper I), we focus on the hot and warm ionized gas properties, by combining high-spatial-resolution radio, X-ray, and optical observations of 25 galaxy groups and clusters. We defer to a future work (Paper II, F. Ubertosi et al. 2025, in preparation) the exploration of the cold molecular phase. We define the sample and present our data analysis techniques in Section 2, and we present the results in Section 3, focusing first on the X-ray gas offsets (Section 3.1) and then on the Hα gas offsets (Section 3.2). We discuss our results in the contexts of the configuration of cool cores (Section 4.1), of the timescales of spatial offset formation (Section 4.2), and of the connection to the SMBH activation (Section 4.3). We then summarize our conclusions in Section 5.

Throughout this work, we assume a ΛCDM cosmology with $H_0 = 70\,\mathrm{km\,s^{-1}/Mpc}$, $\Omega_m = 0.3$, and $\Omega_\Lambda = 0.7$. Uncertainties are reported at 1σ, unless otherwise stated.

2. Sample Selection and Data Analysis

Our primary aim is to study the presence (or absence) of an active SMBH in the presence (or absence) of spatial offsets between the core of the BCG, the X-ray peak of the hot gas, and the emission-line (Hα) peak of the warm gas. As spatial resolution is key, we have based our selection on a combination of Very Long Baseline Array (VLBA), Chandra, and Very Large Telescope (VLT) Multi Unit Spectroscopic Explorer (MUSE) data. We first select systems based on the existence of VLBA observations of central galaxies in galaxy clusters and groups. The milliarcsecond VLBA resolution can unambiguously pinpoint the presence of an active SMBH on parsec scales. Radio observations performed with arcsec-like resolution can also pinpoint AGN activity, but the ~kiloparsec spatial scale sampled by these observations implies that the radio emission could come from cosmic rays accumulated on such scales over relatively long timescales, without tracing ongoing jet ejection (e.g., E. Liuzzo et al. 2009; E. Middelberg et al. 2013; X. Cheng et al. 2025).

We thus consider the VLBA data from projects BE056, BE063, BE065, and BE069, which comprise 5 GHz snapshot observations with a fairly uniform sensitivity and spatial resolution (a few milliarcseconds) of 197 systems (the data for 59 of these were previously presented in M. T. Hogan et al. 2015a, 2015b). Then, we crossmatched the VLBA targets with the Chandra and the VLT/MUSE archives, obtaining a sample of 57 systems with archival observations from these three facilities. By further excluding objects for which Hα emission is not detected in the MUSE cubes, we obtain a compilation of 51 systems. Finally, we apply a redshift cut, limiting this study to systems at $z < 0.2$,[7] which brings us to our final sample of 25 systems (see Table 1 in Appendix A).

We note that as our selection criteria are primarily based on the availability of VLBA, Chandra, and VLT/MUSE data, the resulting sample is unlikely to be statistically complete. However, being targets of radio surveys and dedicated X-ray and optical spectroscopic observations, the 25 systems are likely representative of galaxy groups and clusters where an active radio source, a bright extended X-ray halo, and ionized warm gas are expected. These are typical properties of systems where the feeding and feedback cycle is most relevant, thus aligning with the motivation of this work.

We fully report in Appendix B the data reduction techniques we adopted for the VLBA, MUSE, and Chandra data. These steps allowed us to obtain final maps of the radio emission, on parsec scales, of the hot-gas and of the warm-gas distributions. From these maps, we identified the positions of the SMBH, of the Hα peak, and of the X-ray peak, respectively (see the corresponding relevant subsections in Appendix B). For the VLBA-undetected systems, the position of the SMBH was measured from high-resolution Very Large Array (VLA; radio) or Hubble Space Telescope (HST; optical) imaging (see Appendix B.1 and Table 1 for details). We report in Table 1 the 5 GHz VLBA radio power $P_{5\mathrm{GHz}}$ of the sources in our sample, measured from the peak flux in the VLBA maps and assuming a typical spectral index of $\alpha = -0.7$ (e.g., J. J. Condon et al. 2002). For undetected sources, we report the upper limit on $P_{5\mathrm{GHz}}$ given by $5\sigma_{\mathrm{rms}}$. We also report the R.A., decl. J2000 coordinates of the SMBH, of the X-ray peak, and of the Hα peak.

[7] This cut is motivated by the $0\farcs5$–$1''$ angular resolution of Chandra and MUSE. Existing studies have shown that offsets between warm or hot gas and the BCG are typically on the order of a few kiloparsecs in relaxed systems (S. L. Hamer et al. 2012; T. Pasini et al. 2021; L. Rosignoli et al. 2024). At higher redshifts, the typical angular uncertainty becomes too large to reliably study kiloparsec-scale offsets.

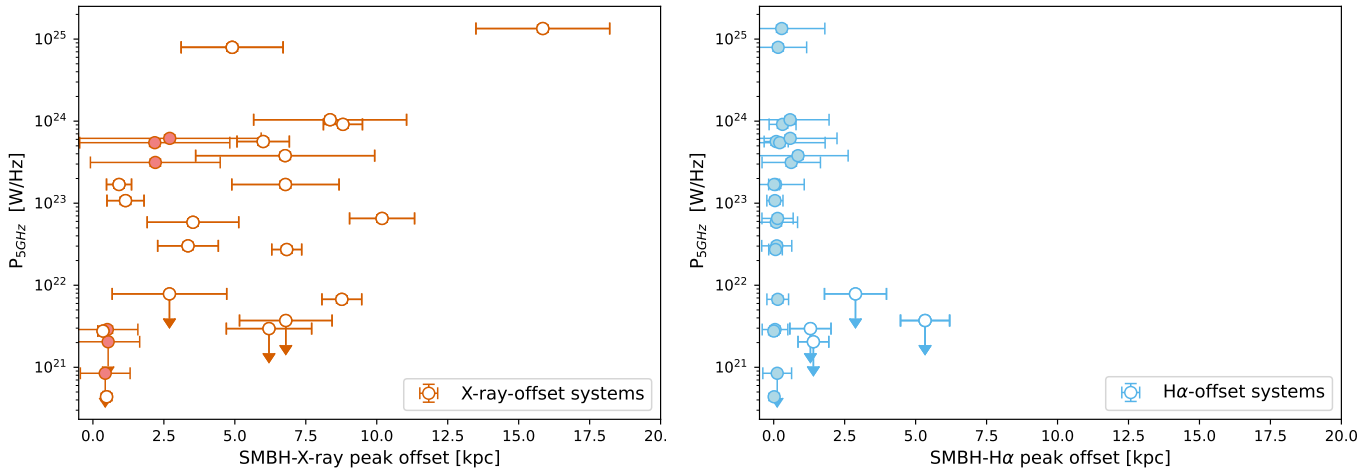

Figure 1. The link between multiphase gas offsets and SMBH activation. Left: radio power at 5 GHz (from parsec-scale VLBA radio observations) of the 25 BCGs in our sample vs. the distance between the positions of the SMBH and of the hot-gas peak (from X-ray emission in Chandra data). Right: radio power at 5 GHz vs the distance between the positions of the SMBH and of the warm-gas peak (from the Hα emission lines in VLT/MUSE data). In both panels, the empty points represent systems with significant offsets (that is, for which the distance Δ between the SMBH and the gas peak is larger than the uncertainty $\delta\Delta$), and the arrows represent the upper limits on the radio power.

We measured the projected physical distance in kiloparsecs between the positions of the SMBH traced by the 5 GHz VLBA data, the peak of the hot gas traced by the X-ray Chandra maps, and the peak of the warm gas traced by the Hα MUSE maps. The results are reported in the last two columns of Table 1. The uncertainties in the offsets Δ were computed as

$$\delta\Delta = \sqrt{\delta_1^2 + \delta_2^2}, \quad (1)$$

where δ_1 and δ_2 are the positional accuracies of the peaks in maps 1 and 2 (see the relevant subsections in Appendix B). The sum of squares is usually dominated by the MUSE or Chandra uncertainty (0.″5–1.″0), as the positional accuracy of VLBA maps (fractions of milliarcseconds) is orders of magnitude smaller.

3. Results

Our primary aim is to relate the multiphase gas offsets to the SMBH quiescent or active state based on the radio power measured in 5 GHz VLBA data (i.e., an undetected radio core provides an upper limit on radio power). To this end, we show in Figure 1 the radio power at 5 GHz of the 25 BCGs in our sample versus the distance between the positions of the SMBH and of the hot (X-ray; left) and warm (Hα; right) gas peaks. We show in Figure 2 and Figure 6 (in Appendix C) the distributions of the hot- and warm-gas phases in the 25 systems of the sample, as well as the locations of the SMBH, the X-ray peak, and the Hα peak.

3.1. SMBH–Hot-gas (X-Ray) Peak Offset

As shown in Figure 1 (left), most systems in our sample (20/25) exhibit significant spatial offsets (that is, for which the distance Δ between the SMBH and the gas peak is larger than the uncertainty $\delta\Delta$) between the positions of the SMBH and the X-ray peak. Quantitatively, the maximum measured offset is $\Delta_{\text{X-ray}}^{\text{SMBH}} = 15 \pm 3$ kpc, with the majority of the systems having their X-ray peak at less than 10 kpc from the SMBH. The average SMBH–X-ray peak offset is 4.7 kpc, with a dispersion of 3.8 kpc. These results are in agreement with literature studies showing that cool-core systems can show $\leqslant$10–20 kpc scale offsets between the core of the BCG and the X-ray peak of the hot gas in cool cores (A. J. R. Sanderson et al. 2009; D. S. Hudson et al. 2010). Moreover, the systems in our sample with a significant X-ray peak offset correspond to about 80% of the total number. This fraction matches the fraction of cool-core clusters where sloshing is taking place (S. Ueda et al. 2020). As noted in Section 1, X-ray peak offsets are typically attributed to bulk motions of the hot gas (e.g., S. L. Hamer et al. 2012), although AGN feedback processes such as uplift might also contribute (L. Rosignoli et al. 2024). In this context, we note that in some systems (NGC 5846, NGC 5044, A3581, and A2052; see Figure 6), the X-ray peak is located along the rims of X-ray cavities, suggesting that AGN-driven uplift can be capable of influencing the hot-gas distribution as much as sloshing, either by pushing the density peak outward or by compressing the gas and locally increasing its density. Finally, we note that there is no evident correlation between the magnitude of the offset and the radio power of the SMBH on parsec scales, and that there appears to be no clear connection between the magnitude of the offset and the radio detection of the SMBH on parsec scales.

3.2. SMBH–Warm-gas (Hα) Peak Offset

The right panel of Figure 1 shows the comparison between the radio power on parsec scales and the Hα peak–SMBH offset. We observe that in most systems (21/25), the Hα peak coincides spatially with the SMBH, while only four systems show significant offsets. The average $\Delta_{\text{H}\alpha}^{\text{SMBH}}$ for the 25 systems is 0.6 kpc, with a standard deviation of 1.4 kpc. The offsets are quite small compared to the X-ray case, up to $\sim$5 kpc at most, being $\Delta_{\text{H}\alpha}^{\text{SMBH}} = 1.4 \pm 0.5$ kpc for A133, $\Delta_{\text{H}\alpha}^{\text{SMBH}} = 1.3 \pm 0.7$ for A2495, $\Delta_{\text{H}\alpha}^{\text{SMBH}} = 2.9 \pm 1.1$ kpc for RX J0821.0+0752, and $\Delta_{\text{H}\alpha}^{\text{SMBH}} = 5.3 \pm 0.9$ kpc for A2566. Most strikingly, all four systems showing an Hα peak–SMBH offset of $\geqslant$1 kpc also lack detected radio cores in VLBA observations, with upper limits on $P_{5\,\text{GHz}}$ of $\leqslant 10^{21-22}$ W Hz^{-1}. This strong correlation suggests that it is the warm gas peaking at the galaxy's center—rather than the

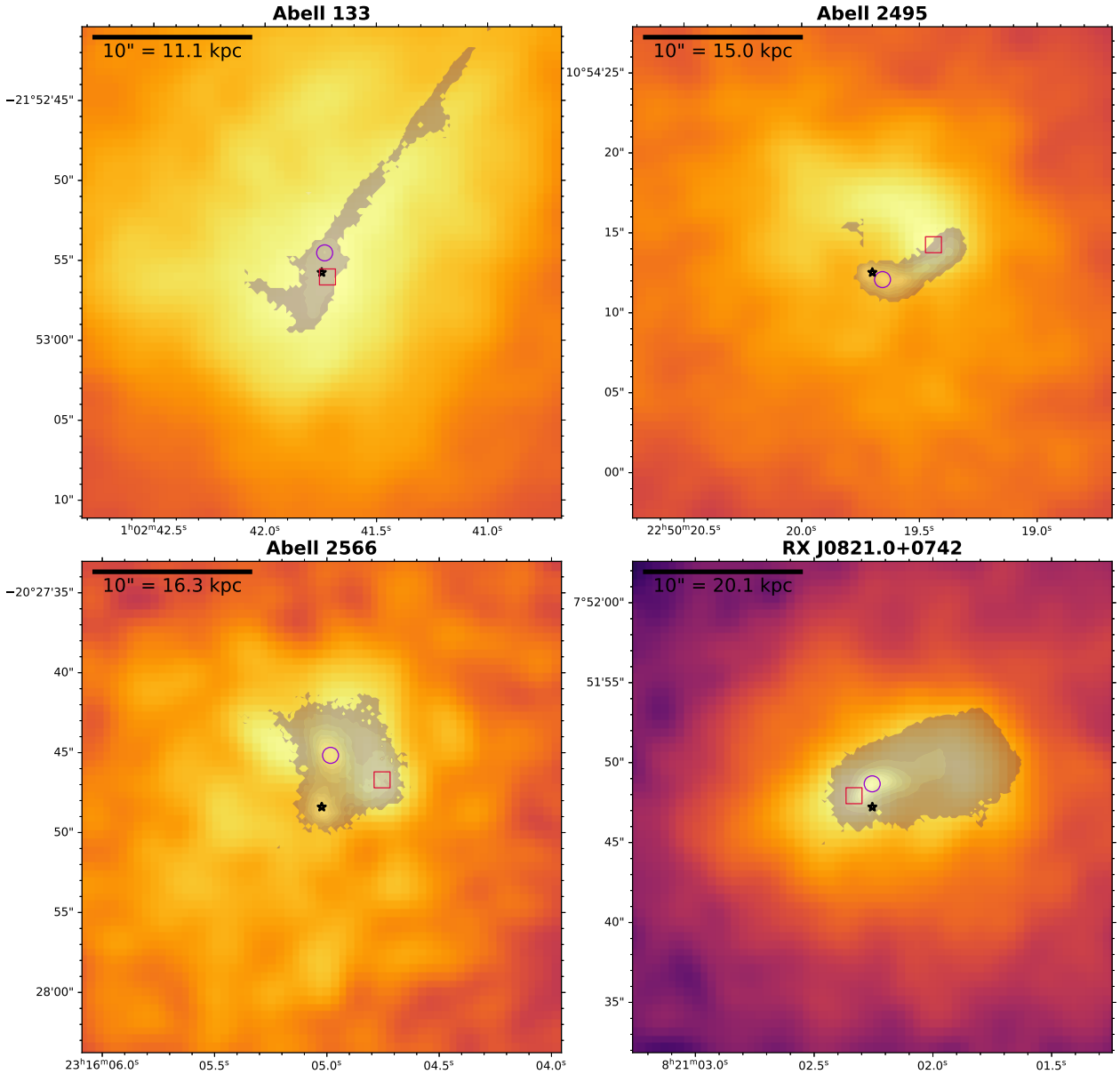

Figure 2. Multiwavelength view of the four systems with a significant Hα peak–SMBH offset. The panels show smoothed X-ray Chandra maps of the hot gas, with grayscale contours of the Hα line from MUSE data. The red square marks the position of the X-ray peak, the purple circle shows the location of the Hα peak, and the black star shows the position of the SMBH (see Table 1).

hot X-ray gas—that plays a decisive role in triggering SMBH activity. We further discuss this scenario in Section 4.

As a note of caution, we considered a potential vicious circle: if the AGNs in our sample were highly efficient at photoionizing the warm gas in their proximity (as in, e.g., Seyferts—G. Kauffmann et al. 2003), then the observed spatial coincidence between the Hα peak and the radio AGN might reflect stronger ionization than in the rest of the nebula rather than a real association with the gas distribution. To test this possibility, we performed a Baldwin, Phillips, and Terlevich (BPT) analysis (e.g., J. A. Baldwin et al. 1981; L. J. Kewley et al. 2001, 2006; G. Kauffmann et al. 2003; R. Cid Fernandes et al. 2010) of the warm-gas emission lines (the details and plots are presented in Appendix D). Although a detailed analysis of the BPT diagrams is outside the scope of the paper, the main findings relevant to this work are summarized as follows: none of the systems exhibit emission consistent with AGN photoionization—instead, the ionization is dominated by a combination of LINER-like and star formation processes, as is commonly seen in BCGs (e.g., K. Fogarty et al. 2015; S. L. Hamer et al. 2016; F. L. Polles et al. 2021). Moreover, there are no significant differences between the ionization conditions at the Hα peak and those across the rest of the nebula, suggesting that the warm gas near the peak shares the same ionization mechanism as the extended filamentary structure.

4. Discussion

4.1. The Fragmentation of Multiphase Gas in Cooling Cores

To highlight the complexity of the spatial relationship between the X-ray peak, the Hα peak, and the SMBH, we show in Figure 3 the comparison between $\Delta_{\mathrm{H}\alpha}^{\mathrm{SMBH}}$ and $\Delta_{\mathrm{X\text{-}ray}}^{\mathrm{SMBH}}$. Within uncertainties, many systems exhibit a noticeable displacement of the X-ray peak relative to the BCG, even

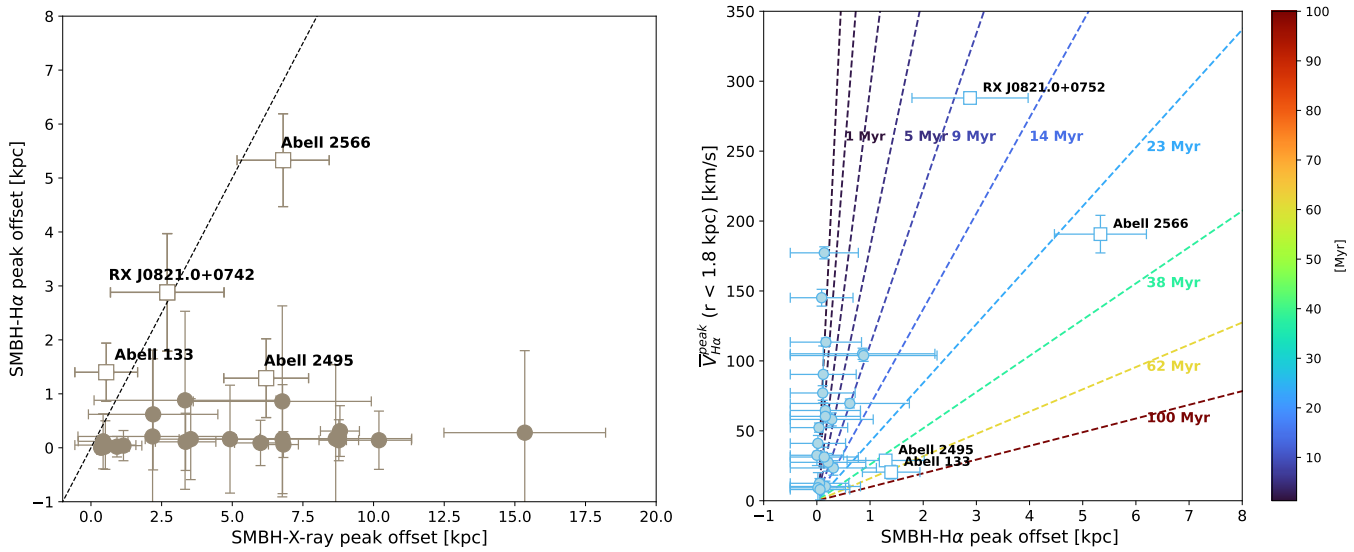

Figure 3. Left: comparison between the SMBH–Hα peak offset and the SMBH–X-ray peak offset; the dashed line marks the line of 1:1 scaling between the two distances. Right: velocity of the warm gas, measured from the MUSE data within an extraction region centered on the Hα peak with radius 1.8 kpc, vs. the SMBH–Hα peak offset. The dashed lines show the times required to traverse the distance on the x-axis at various (constant) velocities on the y-axis. For example, the brown line indicates that for a velocity of 50 km s^{-1}, the time needed to travel a distance of 6 kpc is approximately 100 Myr. Thus, depending on the warm-gas velocity and the offset of the Hα peak from the SMBH, each system lies along a different crossing timeline. In both panels, the open squares represent systems with a significant Hα offset, while the filled circles represent the remaining objects in the sample.

when the Hα emission remains coincident with the galaxy center. Three Hα-offset systems lie along the 1:1 line—in these cases, this plot would suggest an overall alignment of the multiphase gas peaks. However, the picture is more complex. In these systems—RX J0821.0+0752, A2566, and A133—both the Hα and X-ray peaks are offset from the BCG by similar distances, but, as is evident in Figure 2, they are not spatially coincident with each other. In contrast, A2495 has a five-times-larger X-ray peak offset than the Hα one (see also L. Rosignoli et al. 2024). Clearly, these variations demonstrate the diversity in the spatial configurations of cool cores. We stress here that we are not suggesting a complete decoupling between the X-ray and Hα phases. In 22 out of 25 systems, the X-ray peak lies within the Hα nebula (Figures 2 and 6), indicating that an overall spatial association persists. Furthermore, we also find that the Hα peak or the SMBH usually lie within a region of enhanced X-ray emission: Figure 5 shows that in 17 out of the 20 systems with a significant X-ray peak–SMBH/Hα peak offset, the SMBH or the Hα peak still lie within the region where the X-ray emissivity ($\propto n_e^2$) is statistically the highest.

It is difficult to identify the cause of the above diversity. The dynamics of the gas in the systems of our sample is likely influenced by the same physical mechanisms (sloshing due to minor mergers and jet-driven uplift; e.g., E. T. Million et al. 2010; S. L. Hamer et al. 2012; B. R. McNamara et al. 2016). The observed variation among the 25 systems therefore suggests that they are likely being observed at different stages of the same mechanisms driving the offset. For example (see Section 4.2), in some systems, the X-ray and Hα peaks may still be moving away from the SMBH, while in others, they may be falling back toward it.

Additionally, the fact that the X-ray and Hα peaks are not spatially coincident is difficult to reconcile with a simple, yet well-supported, cooling scenario—where different phases of the cooling gas are expected to be cospatial (e.g., B. R. McNamara et al. 2016; M. Gaspari et al. 2017; G. M. Voit et al. 2017). The fact that the X-ray offsets are, on average, larger than the Hα ones is informative, possibly indicating that one phase has decoupled more rapidly than the other from the central potential (see also S. L. Hamer et al. 2012). Due to the typically higher densities and lower temperatures of Hα-emitting filaments compared to those of the hot gas (e.g., V. Olivares et al. 2025), the warm gas may be less easily displaced by hydrodynamic effects (e.g., ram pressure) than the diffuse hot ICM. Clearly, if the warm gas originates from ICM cooling, then the separation must have occurred *after* the warm phase had cooled out of the hot phase—otherwise, the warm-gas peak would also appear offset and coincident with the X-ray peak.

4.2. Timescales of the Warm-gas Offsets

Verifying whether the warm gas cooled out of the ICM before or after the separation occurred would require a reconstruction of the sequence of events, likely through tailored numerical simulations. However, we can still provide a rough estimate of the timescales over which the observed Hα offsets develop and compare these with the hot-gas cooling time. To do so, we use the kinematics of the Hα line, by measuring the average velocity of the warm-gas peak with respect to the redshift of the central galaxy (see Table 1) within a circular aperture of radius 1.8 kpc[8] for each system and plotting it against the projected Hα–SMBH offset in Figure 3 (right). Overlaid on this plot are lines representing the times required to traverse the distance on the x-axis at various velocities. The plot shows that the typical velocities in systems with a coincident Hα peak and SMBH range between 0 and 200 km s^{-1}. The four Hα-offset systems cover a wide parameter space in this plot, reflecting once again the diversity in cooling cores. Notably, the two systems with the smallest

[8] The smallest physical scale consistently probed across our sample is set by the largest uncertainty in the measured distance between the Hα peak and the SMBH, approximately 1.8 kpc.

offsets (∼1.3 kpc; A2495 and A133) also exhibit the lowest velocities (∼20–30 km s^{-1}), while the two with the largest offsets (∼3–5 kpc; A2566 and RX J0821.0+0752) show the highest velocities (∼200–300 km s^{-1}). This trend may support a scenario in which, when the Hα peak is displaced from the SMBH, stronger bulk motions produce greater separations between gas components. However, there are at least two caveats. The first is that any motion (whether due to sloshing or AGN-driven uplift) is unlikely to occur at constant velocity. In sloshing scenarios, for example, the gas likely follows an oscillatory trajectory, with the velocities varying along the path (e.g., R. E. Johnson et al. 2012). Statistically, one would expect the velocity to be smallest at the largest offsets (i.e., near apocenter) and highest near the smallest offsets (pericenter), which would produce the opposite trend to what is observed for the four Hα-peak-offset systems. The second and possibly most relevant one is that projection effects are likely significant (see Figure 6). A133 and A2495 show narrow elongated Hα morphologies, suggesting motion predominantly in the plane of the sky (e.g., N. A. Hatch et al. 2006). In these cases, the observed offset may closely approximate the 3D displacement, while the line-of-sight velocity might underestimate the 3D velocity—meaning these systems would shift upward in Figure 3 (right), implying shorter timescales. Conversely, A2566 and RX J0821.0+0752 exhibit rounder Hα morphologies and high $\bar{V}_{\rm H\alpha}^{\rm peak}$, consistent with nonnegligible motion along the line of sight. For these systems, the true 3D spatial offsets may exceed the projected values, implying longer timescales (i.e., a shift to the right in the plot). Taken together, these geometrical considerations suggest that all four systems likely lie along similar time tracks ($t_{\rm offset} \sim$ 20–40 Myr). Nevertheless, because the true 3D geometry is not directly measurable, we adopt the projected quantities shown in Figure 3 (right) and conclude that the characteristic timescales over which these offsets develop range from approximately 10–70 Myr. We note that the observed timescales are comparable to the typical freefall time of gas at $r \leqslant 6$ kpc within a 10^{10}–$10^{11}\,M_{\odot}$ galaxy ($t{\rm ff} \propto r^{3/2} \times M^{-1/2} \lesssim 25$ Myr), suggesting that the warm gas may be moving ballistically. At the same time, these timescales are longer than the typical sound-crossing time at the same radius in gas with $0.5 \leqslant kT$, [keV] $\leqslant 5$ ($t_{\rm sc} \propto r \times kT^{-1/2} \lesssim 15$ Myr), which is consistent with subsonic motions of the hot gas (e.g., Y. Su et al. 2017). Moreover, the timescales are shorter than the central cooling time $t_{\rm cool} \propto T^{1/2} n_e^{-1}$ of the X-ray gas (∼400 Myr for A133—K. W. Cavagnolo et al. 2009; ∼350 Myr for A2495—L. Rosignoli et al. 2024; ∼400 Myr for A2566—from the temperature and density values in S. K. Kadam et al. 2024; ∼350 Myr for RX J0821.0+0752—A. N. Vantyghem et al. 2019). Therefore, the fact that the X-ray peak is offset from the warm-gas peak is not in contrast with a cooling origin—the warm- and hot-gas phases may have detached from one another after condensation.

4.3. Connection to the SMBH Activation

Our analysis of Section 3 showed that all four systems exhibiting a spatial offset between the Hα peak and the SMBH also show no detectable VLBA radio cores, with upper limits on their radio power of $P_{5\,\rm GHz} \leqslant 10^{21-22}$ W Hz^{-1}. The absence of radio-bright jets in Hα-offset systems suggests that the central concentration of warm gas plays a key role in sustaining powerful SMBH activity. This observational coincidence may support the idea that the mode of accretion in central galaxies is not dominated by the accretion of hot gas at the Bondi rate (H. Bondi 1952; see, e.g., S. W. Allen et al. 2006; Y. Fujita et al. 2016; D. Prasad et al. 2024) but instead by the intermittent infall of cooled gas clouds condensed out of the ICM (e.g., F. Pizzolato & N. Soker 2005; M. Gaspari et al. 2013; G. M. Voit et al. 2017; see also H. R. Russell et al. 2013; C. J. Bambic et al. 2023 for detailed discussions). Our results seem to suggest that warm gas, when peaking near the SMBH, provides a sufficient fuel reservoir to enhance the accretion rate and trigger jet formation, which results in a relatively high parsec-scale radio power of the SMBH ($P_{5\,\rm GHz}$ up to 10^{24-25} W Hz^{-1}; see Figure 1). This aligns with theoretical models of cold accretion, where cold molecular gas (originating from the warm phase) primarily fuels the SMBH (F. Pizzolato & N. Soker 2005; M. Gaspari et al. 2013, 2017; G. M. Voit et al. 2017).

Our conclusion on the inactive state of the SMBHs in the four Hα-offset systems is additionally supported by existing studies of AGN feedback (i.e., the presence of X-ray cavities) in these objects. In A2495, the detected cavities seem associated with past outbursts that are now fading (see T. Pasini et al. 2019; L. Rosignoli et al. 2024); the cavities are also asymmetric with respect to the X-ray peak. In A133, cavities are detected on one side of the X-ray peak, at large radii (∼60 kpc), and cospatial with remnant, aged radio emission, consistent with diffuse bubbles that likely detached long ago (see S. W. Randall et al. 2010). In A2566, no clear cavities are visible in the Chandra data, and the dedicated analysis by S. K. Kadam et al. (2024) does not report any. Finally, in RXJ 0821+0752, one depression is found on one side of the core (see C. M. Bayer-Kim et al. 2002; A. N. Vantyghem et al. 2019). If interpreted as a cavity, this feature would most likely trace a fading past outburst, given the lack of associated extended radio emission. Taken together, these results indicate that jet feedback has indeed been ongoing in these systems, but primarily in the past, since the observed cavities are all linked to fading outbursts. This supports our conclusion that no major AGN fueling episode has occurred in recent times (within a few Myr, i.e., the typical age of young X-ray cavities).

For clarity, we stress that we are not suggesting that all Hα-offset systems have an inactive SMBH but only that any core radio emission is too faint to be detected at current VLBA sensitivities. If future studies identify cases of VLBI-detected SMBHs in central galaxies with offset Hα peaks, our results suggest that such systems will be characterized by very low radio powers. However, this prediction is sensitive to the timescales. As shown in Figure 3, depending on the combination of the spatial distance and warm-gas velocity, the timescales might be short enough to allow periodic passages of the Hα peak near the SMBH, the deposition of fuel, and the maintenance of AGN activity (see also L. Rosignoli et al. 2024). The relevant timescale to match is the synchrotron cooling timescale of relativistic electrons, which depends on the frequency and magnetic field strength as $t_{\rm syn} \propto \nu^{-1/2} B^{-3/2}$ (e.g., M. S. Longair 2011). For magnetic field strengths typical of parsec-scale radio jets (i.e., $B \geqslant 0.1$ mG; e.g., C. Xu et al. 2000; D. Dallacasa et al. 2021), the cooling time at GHz frequencies is $t_{\rm syn} \leqslant 5$ Myr. Therefore, if an offset event occurred within the past few Myr, the SMBH could still show radio emission on parsec scales.

Finally, we return to our four Hα-offset VLBA-undetected systems and consider a case in which future, deeper VLBI observations reveal emission with radio power just below our upper limits. First, we note that in all four systems with offset Hα peaks, the SMBH is still embedded in the extent of the warm-gas nebula (see Figure 6; in A2566, a secondary Hα blob is also present at the SMBH location), suggesting that some fuel might still be available—though seemingly not enough to support radio powers exceeding 10^{22} W Hz^{-1}. Second, we note that even a VLBI detection may not imply that these systems host jets. At low radio powers, other mechanisms can become the dominant origin of synchrotron emission (e.g., see F. Panessa et al. 2019 for a review). For the case of VLBI scales, and considering the early-type galaxies at the centers of clusters and groups, the most likely alternative synchrotron source is the advection-dominated accretion flow (ADAF) surrounding the SMBH (e.g., A. Doi et al. 2011; F. Panessa et al. 2019; see also G. Schellenberger et al. 2024 for an example of ADAF emission in a central group galaxy). The maximal ADAF radio power at a given frequency is a function of the SMBH mass (e.g., Q. Wu & X. Cao 2005), with the dependence at 5 GHz being $P_{\rm ADAF} \propto M_{\rm BH}^{1.25}$. Based on the K-band magnitudes of their host galaxies (A. W. Graham 2007), the SMBHs in the four Hα-offset systems have masses of 1–2 $\times$ 10^9 $M_\odot$, implying a maximum ADAF radio power at 5 GHz of about 1–3 $\times$ 10^{21} W Hz^{-1}. These values are just below our current 5σ upper limits (see Table 1). Thus, if future high-sensitivity VLBI observations reveal faint (and unresolved) radio emission in these systems, it is still possible that this could arise from an ADAF rather than a jet.

5. Summary

In this work, we have explored the spatial offsets between the multiphase gas around central galaxies, and their connection to the SMBH activation, in a sample of 25 cool-core galaxy groups and clusters. Our strategy has combined observations from some of the highest-angular-resolution instruments available in their respective bands: Chandra for the X-ray-emitting hot gas, VLT/MUSE for the optical emission lines tracing the warm gas, and VLBA for parsec-scale radio emission from the AGN. Our results can be summarized as follows:

1. On average, the offsets between the X-ray peak and the SMBH ($\langle \Delta^{\rm SMBH}{\rm X\text{-}ray} \rangle = 4.8$ kpc) are significantly larger than those between the Hα peak and the SMBH ($\langle \Delta^{\rm SMBH}{\rm H}\alpha \rangle = 0.6$ kpc). There is also a higher incidence of X-ray offsets ($\sim$80%) than of Hα offsets ($\sim$15%). This evidence supports a scenario in which gas sloshing primarily drives these displacements, with the denser warm phase being more difficult to separate from the central galaxy than the diffuse hot halo.
2. The spatial configuration of multiphase gas in cooling cores shows a large degree of variation. While the extent of the warm ionized nebula often overlaps with the location of the X-ray peak, the peak of the Hα emission is rarely coincident with it. This evidence can still be reconciled with a cooling scenario—where the warm gas cools out of the hot gas—by considering the relevant timescales. Our data indicate that offsets between the Hα peak and the SMBH develop on timescales of 10–70 Myr, significantly shorter than the typical cooling time of the central hot gas (300–400 Myr). This suggests that the warm- and hot-gas phases may have detached from one another after condensation.
3. A striking result emerges from our study of how the X-ray and Hα offsets relate to SMBH activation. While there is no apparent correlation between the magnitude of the X-ray offset and the radio power of the SMBH, all four systems showing an Hα peak–SMBH offset of $\geqslant$1 kpc also lack detected radio cores, with upper limits on $P_{5\ \rm GHz}$ of $\leqslant 10^{21-22}$ W Hz^{-1}. In the remaining 21 systems, the parsec-scale radio powers can reach $P_{5\ \rm GHz} \sim 10^{24-25}$ W Hz^{-1}. These results suggest that a central concentration of warm gas plays an important role in sustaining powerful SMBH activity. This, in turn, supports the idea that cold-mode accretion contributes to fueling AGN with relatively high radio power.

In an upcoming paper (Paper II, F. Ubertosi et al. 2025, in preparation), we will expand this analysis to the cold molecular phase, which represents the end product of the multiphase cooling cascade and, according to cold-accretion models, is the most closely related to AGN fueling. We also highlight that this analysis would not have been possible without the high spatial resolution provided by the Chandra X-ray telescope, matching that of VLT/MUSE. The future of multiphase gas studies relies on maintaining such capabilities, either through the continued operation of Chandra or through next-generation observatories. In this context, the Advanced X-ray Imaging Satellite (see C. S. Reynolds et al. 2023), with its proposed 1.″5 angular resolution, represents a promising successor for high-resolution X-ray imaging of galaxy cluster cores.

Acknowledgments

The authors sincerely thank the anonymous referee for providing a clear and constructive report on our manuscript. F. U. thanks the Smithsonian Astrophysical Observatory for the hospitality and support during his visits in 2024 and 2025, during which periods this project was developed and finalized, respectively. F.U. thanks E. Giunchi for the useful discussion on optical data analysis. F.U. and M.G. acknowledge support from the research project PRIN 2022 "AGN-sCAN: zooming-in on the AGN–galaxy connection since the cosmic noon," contract 2022JZJBHM_002—CUP J53D23001610006. E.O.S. acknowledges support from the Smithsonian Combined Support for Life on a Sustainable Planet, Science, and Research administered by the Office of the Under Secretary for Science and Research, and from the National Aeronautics and Space Administration (NASA) through Chandra Award Number GO4-25079X issued by the Chandra X-ray Center, which is operated by the Smithsonian Astrophysical Observatory for and on behalf of NASA under contract NAS8-03060. G.S. acknowledges support from the Chandra High Resolution Camera Project through NASA contract NAS8-03060. G.S. also acknowledges support through Chandra grant AR4-25011X. P.T. acknowledges support from NASA's NNH22ZDA001N Astrophysics Data and Analysis Program under award 24-ADAP24-0011. The National Radio Astronomy Observatory is a facility of the National Science Foundation, operated under cooperative agreement by Associated Universities, Inc. Based on data obtained from

the ESO Science Archive Facility: European Southern Observatory (ESO; 2016). This research has made use of a list of Chandra data sets, obtained by the Chandra X-ray Observatory, contained in the Chandra Data Collection (CDC): doi:10.25574/cdc.470. Basic research in radio astronomy at the Naval Research Laboratory is supported by 6.1 base funding.

Author Contributions

F.U. developed the research concept, analyzed the data, and was responsible for writing and submitting the manuscript. G. S. and E.O.S. developed the idea of analyzing a large collection of VLBA observations of central galaxies. E.O.S. provided funding to support the publication of the manuscript. F.B. provided extensive support on the data analysis and interpretation. All coauthors contributed equally to the review of this manuscript.

Facilities: NRAO (VLBA), CXO, VLT:Yepun (MUSE).

Software: `AIPS` (E. W. Greisen 1990, 2003), CASA (J. P. McMullin et al. 2007), CIAO (A. Fruscione et al. 2006), PLATEFIT (C. A. Tremonti et al. 2004).

Appendix A
The Sample

We report in Table 1 the list of 25 systems selected for our study (ordered by increasing redshift), along with the positions of the SMBH, of the X-ray peak, and of the Hα peak. We also report the spatial offsets between the different components.

Table 1
Measured Properties for the 25 Objects in Our Sample, Ordered by Increasing Redshift

Name	z	$P_{5\mathrm{GHz}}$ (10^{22} W Hz^{-1})	SMBH	X-Ray Peak	Hα Peak	$\Delta X_{\mathrm{X\text{-}ray}}^{\mathrm{SMBH}}$ (kpc)	$\Delta X_{\mathrm{H}\alpha}^{\mathrm{SMBH}}$ (kpc)
NGC 5846	0.00572	0.040 ± 0.004	15:06:29.2917 +1:36:20.342	15:06:29.0231 +1:36:20.828	15:06:29.2945 +1:36:20.473	0.48 ± 0.12	0.02 ± 0.06
NGC 5044	0.009	0.28 ± 0.03	13:15:23.9613 −16:23:07.549	13:15:24.0621 −16:23:06.255	13:15:23.9627 −16:23:07.529	0.36 ± 0.18	0.00 ± 0.12
A3581	0.02179	16.9 ± 1.7	14:07:29.7622 −27:01:04.293	14:07:29.8564 −27:01:05.952	14:07:29.7639 −27:01:04.323	0.92 ± 0.44	0.02 ± 0.19
NGC 7237	0.02621	2.7 ± 0.3	22:14:46.8819 +13:50:27.115	22:14:46.0953 +13:50:21.129	22:14:46.8739 +13:50:27.150	6.81 ± 0.53	0.06 ± 0.24
A496	0.03273	10.8 ± 1.1	04:33:37.8413 −13:15:42.989	4:33:37.7749 −13:15:41.566	04:33:37.8357 −13:15:43.016	1.15 ± 0.65	0.04 ± 0.28
A2052	0.03453	91.4 ± 9.1	15:16:44.5130 +7:01:18.100	15:16:43.6611 +7:01:19.779	15:16:44.4943 +7:01:17.731	8.81 ± 0.69	0.31 ± 0.47
ZwCl 0335+0956	0.03520	0.67 ± 0.07	3:38:40.5505 +9:58:12.042	3:38:41.0218 +9:58:01.585	3:38:40.5557 +9:58:11.853	8.77 ± 0.70	0.14 ± 0.38
ACT-CL J1521.8+0742[a]	0.04419	⩽0.08	15:21:51.8509 +7:42:31.831	15:21:51.8860 +7:42:32.015	15:21:51.8545 +7:42:31.703	0.43 ± 0.88	0.12 ± 0.51
A1644	0.047	56.4 ± 7.4	12:57:11.5961 −17:24:34.135	12:57:11.9829 −17:24:30.740	12:57:11.6007 −17:24:34.166	6.00 ± 0.92	0.09 ± 0.42
A2626	0.055	3.0 ± 0.4	23:36:30.4916 +21:08:47.460	23:36:30.5021 +21:08:50.607	23:36:30.4939 +21:08:47.557	3.35 ± 1.07	0.11 ± 0.53
A85	0.05536	0.29 ± 0.03	0:41:50.4696 −9:18:11.394	0:41:50.4974 −9:18:11.656	0:41:50.4661 −9:18:11.399	0.51 ± 1.08	0.05 ± 0.45
A133[a]	0.057	⩽0.20	1:02:41.7460 −21:52:55.757	1:02:41.7175 −21:52:56.057	1:02:41.7328 −21:52:54.536	0.54 ± 1.11	1.40 ± 0.54
A1991	0.05921	6.5 ± 0.7	14:54:31.4879 +18:38:32.413	14:54:31.4247 +18:38:41.231	14:54:31.4871 +18:38:32.521	10.19 ± 1.15	0.14 ± 0.54
A2495[b]	0.0794	⩽0.30	22:50:19.700 +10:54:12.526	22:50:19.4448 +10:54:14.254	22:50:19.6567 +10:54:12.075	6.20 ± 1.50	1.29 ± 0.73
A478	0.086	5.9 ± 0.6	4:13:25.2778 +10:27:54.777	4:13:25.1296 +10:27:54.930	4:13:25.2677 +10:27:54.786	3.53 ± 1.61	0.16 ± 0.75
A2566[c]	0.0871	⩽0.37	23:16:05.0230 −20:27:48.400	23:16:04.7542 −20:27:46.701	23:16:04.9838 −20:27:45.169	6.80 ± 1.63	5.33 ± 0.86
MCXC J1558.3-1410	0.097	793.5 ± 79.4	15:58:21.9481 −14:09:59.052	15:58:21.8052 −14:09:57.276	15:58:21.9482 −14:09:58.969	4.92 ± 1.80	0.16 ± 1.00

Table 1
(Continued)

Name	z	$P_{5\mathrm{GHz}}$ (10^{22} W Hz^{-1})	SMBH	X-Ray Peak	Hα Peak	$\Delta X_{\mathrm{X\text{-}ray}}^{\mathrm{SMBH}}$ (kpc)	$\Delta X_{\mathrm{H}\alpha}^{\mathrm{SMBH}}$ (kpc)
PKS 0745-191	0.1028	16.9 ± 1.7	7:47:31.3264 −19:17:39.986	7:47:31.0735 −19:17:40.013	7:47:31.3230 −19:17:39.910	6.78 ± 1.89	0.16 ± 1.01
RX J0821.0+0752[d]	0.11007	⩽0.78	8:21:02.2550 +7:51:47.222	8:21:02.3319 +7:51:47.907	8:21:02.2555 +7:51:48.672	2.70 ± 2.01	2.88 ± 1.09
A1664	0.12798	31.4 ± 5.8	13:03:42.5652 −24:14:42.216	13:03:42.5658 −24:14:41.312	13:03:42.5658 −24:14:42.484	2.20 ± 2.29	0.62 ± 1.03
RX J1350.3+0940	0.13255	1345 ± 140	13:50:22.1360 +9:40:10.656	13:50:21.6860 +9:40:09.878	13:50:22.1428 +9:40:10.724	15.35 ± 2.86	0.28 ± 1.52
A2204	0.152	54.7 ± 5.5	16:32:46.9447 +5:34:32.747	16:32:46.8972 +5:34:32.364	16:32:46.9425 +5:34:32.679	2.18 ± 2.64	0.21 ± 1.60
MCXC J2014.8-2430	0.1555	104.0 ± 11.4	20:14:51.7332 −24:30:22.723	20:14:51.5104 −24:30:23.007	20:14:51.7376 −24:30:22.522	8.66 ± 2.69	0.17 ± 1.37
A383	0.18884	38.0 ± 4.6	2:48:03.3955 −3:31:44.856	2:48:03.3037 −3:31:46.521	2:48:03.3904 −3:31:44.963	6.77 ± 3.15	0.86 ± 1.77
MCXC J0331.1-2100	0.19276	61.7 ± 9.9	3:31:06.0316 −21:00:33.018	3:31:05.9913 −21:00:32.467	3:31:06.0394 −21:00:33.006	3.33 ± 3.22	0.88 ± 1.65

Notes. Column (1): name. Column (2): redshift. Column (3): 5 GHz radio power from the VLBA data, measured from the peak flux in the VLBA maps—upper limits are given at $5\sigma_{\mathrm{rms}}$ (see Section 2). Column (4): coordinates of the SMBH from VLBA data (see notes for nondetections as well as Appendix B.1). Column (5): coordinates of the X-ray peak from Chandra data (see Appendix B.3). Column (6): coordinates of the Hα peak from MUSE data (see Appendix B.2). Column (7): spatial offset between the SMBH and the X-ray peak. Column (8): spatial offset between the SMBH and the Hα peak.

[a] SMBH located in archival VLA images at 1.4 GHz (see the NVAS project), with positional accuracy of 0.″12 (10% of the beam FWHM).

[b] SMBH located in archival VLA images at 4.8 GHz (T. Pasini et al. 2019), with positional accuracy of 0.″1 (10% of the beam FWHM).

[c] SMBH located in VLASS images at 3.0 GHz, with positional accuracy of 0.″2 (see the VLASS continuum user guide).

[d] SMBH located in HST images (A. N. Vantyghem et al. 2019), with positional accuracy of 0.″1.

Appendix B
Data Reduction and Analysis

B.1. VLBA Data

We reduced the VLBA data using standard reduction techniques in `AIPS`,[9] including the correction for the Earth orientation parameters and ionospheric delays, the application of digital sampling corrections, the removal of instrumental delays in phases, the bandpass calibration, and the correction for time-dependent delays in phases. Ultimately, we applied the calibration and averaged channels in the different spectral windows. No self-calibration was performed on the target visibilities, to avoid losing the information on the absolute position. Imaging was performed in `AIPS` adopting Briggs (D. S. Briggs 1995) weighting (with `robust = 0`). Since the phase center of the data did not always match the exact position of the radio core, we imaged the whole field of view (a few arcseconds) to secure the identifications of sources far from the phase center. For the 19 detections, the peaks in the maps were used as tracers for the positions of the SMBHs.[10] For the five nondetections, we considered the positions of the radio cores in high-resolution VLA imaging (for ACT-CL J1521.8+0742, A133, A2495, and A2566) or of the BCG optical peak in HST imaging (for RX J0821.0+0752), both of which have positional accuracies of ∼0.″1, as tracers of the positions of the SMBHs (see the details in Table 1). To check for potential biases in using these alternative methods to locate the SMBHs in VLBA-undetected systems, we proceeded with the following validation procedures:

1. To validate the high-resolution VLA imaging method, we considered the 20 VLBA detections in our sample and compared the positions of the radio cores in the VLBA images with the positions of the radio cores in 3 GHz images from the Very Large Array Sky Survey (VLASS),[11] which has a typical positional uncertainty of 0.″2, comparable to that of the VLA images we employed (see the notes in Table 1). The comparison shown in Figure 4 (left) demonstrates that the lower-resolution radio images provide good tracers of the positions of the SMBHs, as the distribution is centered around zero with a standard deviation in δR.A., δdecl. $= 0.''16$ (consistent with the VLASS positional accuracy, ∼0.″2).
2. To validate the HST imaging method, we considered the 11 VLBA detections in our sample with available HST images in the archive[12] (NGC 5846, NGC 5044, A3581, NGC 7237, A496, A2052, ZwCl 0335+0956, A2626, A478, PKS 0745-191, and A2204) and compared the

[9] https://www.aips.nrao.edu/.

[10] Possible core-shift effects or self-absorption masking the true core (e.g., K. V. Sokolovsky et al. 2011) introduce systematic errors of ∼0.1″ at most, which are very negligible with respect to the Chandra and MUSE resolutions.

[11] See https://science.nrao.edu/vlass/data-access/vlass-epoch-1-quick-look-users-guide.

[12] See https://hla.stsci.edu/.

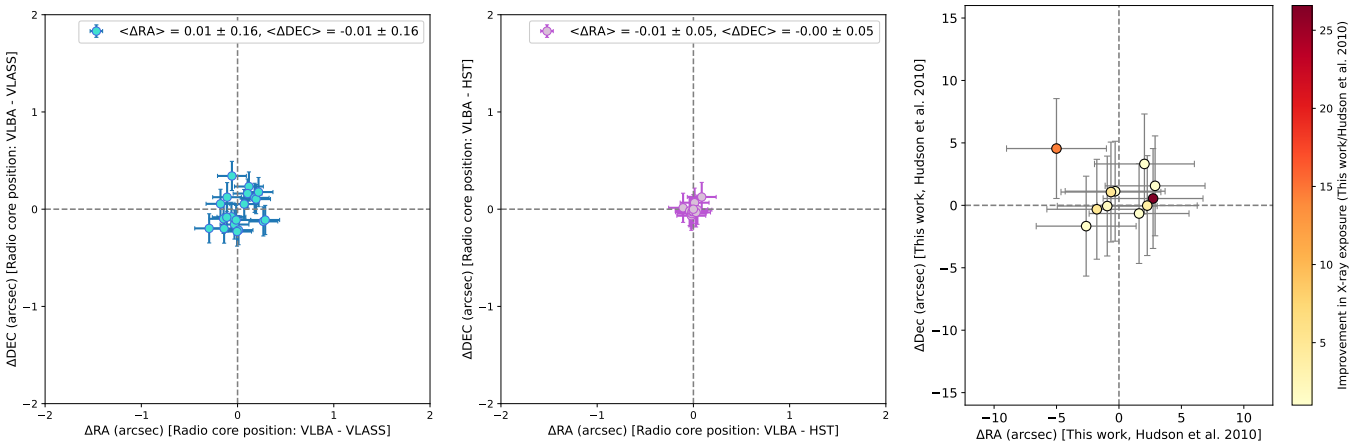

Figure 4. Left: comparison between the positions of the radio cores in VLBA images and those in VLASS 3 GHz images for the 20 systems with VLBA detections (see Appendix B.1). The distribution is centered near zero, with a dispersion of $\sim 0\farcs16$, consistent with the VLASS positional accuracy ($\sim 0\farcs2$). As noted in Appendix B.1, this supports using VLA observations to estimate SMBH positions in VLBA-undetected systems (i.e., ACT-CL J1521.8+0742, A133, A2495, and A2566). Center: comparison between the positions of the radio cores in VLBA images and the optical peaks of the galaxies in HST images for the 11 systems with both VLBA detections and available HST data (see Appendix B.1 for details). The distribution is centered around zero, with a dispersion of approximately $0\farcs05$—comparable with the positional accuracy of HST ($\leqslant 0\farcs1$). As discussed in Appendix B.1, this validates the use of HST imaging to locate the SMBHs in VLBA-undetected systems (i.e., RX J0821.0+0752). Right: comparison between the X-ray peak positions reported in this work (Table 1) and those from D. S. Hudson et al. (2010) for 11 overlapping systems (see Appendix B.3). Points are color-coded by the ratio of the Chandra exposure times in this work and those of D. S. Hudson et al. (2010). As detailed in Appendix B.3, the agreement validates our X-ray peak identification method. The only outlier is A3581, with an offset of ΔR.A. $= 5\farcs2 \pm 4\farcs1$ and Δdecl. $=4\farcs9 \pm 4\farcs1$, which is likely explained by the 15 times deeper exposure used in our analysis.

positions of the radio cores in the VLBA images with the positions of the BCG optical peaks. The comparison shown in Figure 4 (middle) demonstrates that the HST images provide good tracers of the positions of the SMBHs, as the distribution is centered around zero with a standard deviation in δR.A., δdecl. $= 0\farcs05$ (comparable with the positional accuracy of HST, $\leqslant 0\farcs1$).

Based on these tests, we are confident that using VLA images (for ACT-CLJ1521.8+0742, A133, A2495, and A2566) or HST images (for RX J0821.0+0752) to estimate the SMBH positions in VLBA-undetected systems does not introduce systematic biases in our results.

B.2. VLT/MUSE Data

We present optical nebular emission-line maps for the 25 sources in our sample from an analysis of data obtained with MUSE. The MUSE data were reduced using the standard recipes provided by the MUSE pipeline (P. M. Weilbacher et al. 2014). Then, we checked the astrometry of the cubes, by checking the coordinates of the detected sources against external catalogs (PanSTARRS and GAIA). When necessary, we corrected the cubes for any astrometric shift, which we found to be always smaller (below $0\farcs3$) than the average seeing ($\sim 0\farcs8$). We fitted the data following the same method described by V. Olivares et al. (2019)—that is, using `PLATEFIT`[13] (C. A. Tremonti et al. 2004) to simultaneously fit the stellar continuum and emission lines. We imposed a threshold in the signal-to-noise ratio (SNR) of 3 for the detection of emission lines, and we produced maps of Hα intensity (see Figures 2 and 6). The position of the warm-gas peak corresponds to the pixel with the largest Hα flux. The uncertainty on the location of the Hα peak is given by the seeing of the observation. The velocities of the warm-gas peaks, traced by the Hα lines and shown in Figure 3, are measured relative to the redshift of the central galaxy (see Table 1).

B.3. Chandra Data

We retrieved ACIS data from the Chandra archive[14] and reprocessed the observations using `CIAO-4.16`;[15] for each object, we restricted the analysis to all the available observations obtained with ACIS-S and ACIS-I, without gratings. The data were reprocessed with the `chandra_repro` script; for each object with multiple ObsIDs, the astrometry of each ObsID was matched to that of the longest ObsID. We filtered the data from periods contaminated by background flares. Blank-sky event files were selected as background files and normalized by the 9–12 keV count rate of the observation. Then, we merged the event files and the background images, obtaining mosaicked images for the target source and the background in the 0.5–7 keV band. For each target, we verified if the astrometry of the Chandra mosaic needed further corrections beyond its nominal pointing accuracy ($0\farcs4$) and proceeded to update the coordinates, when necessary. As the peak in the X-rays can be dominated by nonthermal emission from point sources in the image (the BCG itself, in some cases; H. R. Russell et al. 2013), we first identified point sources in the mosaics with `wavdetect` and masked them by interpolating the counts from an annular region surrounding the point source and extending to 1.5 times its extent. Then, to mitigate potential pixel-to-pixel variations (especially in the low-count regime), we convolved the maps with a $1\farcs0$ FWHM Gaussian (see also D. S. Hudson et al. 2010). Ultimately, we identified the X-ray brightest pixel in the map and considered a $0\farcs5$ radius as the uncertainty on the location of the X-ray peak.

To validate our method of identifying the X-ray peak, we compare our results with those of D. S. Hudson et al. (2010), focusing on the 11 systems common to both samples. For each system, we considered the X-ray peak positions from our work (Table 1) and from Table 2 in D. S. Hudson et al. (2010), then computed the angular offset in R.A. and decl. between the two

[13] https://pyplatefit.readthedocs.io/en/latest/.

[14] cda.harvard.edu/chaser

[15] https://cxc.cfa.harvard.edu/ciao/.

sets. We note that D. S. Hudson et al. (2010) convolved the Chandra maps with a $8\farcs0$ FWHM Gaussian, therefore we considered a $4''$ radius as the uncertainty on their location of the X-ray peak. We show the comparison in Figure 4 (right), where each point is color-coded according to the ratio of the Chandra exposure time used in our analysis to that used in the earlier study. This is meant to provide context for interpreting the agreement (longer exposures yield better SNRs and potentially more accurate peak localizations). We find a good agreement between our study and that of D. S. Hudson et al. (2010), since the distribution is centered at zero and $10/11$ systems are consistent with $0''$ difference. The only outlier is A3581, with an offset of $\Delta\mathrm{R.A.} = 5\farcs2 \pm 4\farcs1$ and $\Delta\mathrm{decl.} = 4\farcs9 \pm 4\farcs1$. This is explained by the 15 times deeper Chandra exposure we employed ($\sim$90 ks here versus $\sim$6 ks in D. S. Hudson et al. 2010), which likely provides a more accurate localization of the X-ray peak.

For completeness, we also explored a statistical approach based on Poisson fluctuations in the count rate to estimate the positional uncertainty of the X-ray peak. For each system, we defined a "statistical confidence region," centered on the X-ray peak, by selecting all pixels with counts greater than $N_C^P - \sqrt{N_C^P}$, where N_C^P is the number of counts in the brightest pixel of the map. This threshold encompasses all pixels statistically consistent with the brightest one, under the assumption of Poisson statistics. We show in Figure 5 the X-ray images where we overlay contours corresponding to this threshold. In systems with low surface brightness, such as ACT-CL J1521.8+0742 and A1644, where the peak pixel count is below 1 count per pixel, the resulting confidence region formally extends to the edge of the image. In the other systems, the extent of this region depends on the total number of counts within the X-ray peak and on how peaked the surface brightness distribution is. This alternative method allows us to visualize the extent of the region where the X-ray peak might be statistically located with the current X-ray exposure. However, in our analysis, we keep the $0\farcs5$ radius uncertainty (see above), because of the following reasons: (1) the "statistical confidence region" does not provide a more physically motivated indication of where the density peak (and thus the cooling peak) might be located; (2) the use of a fixed positional uncertainty based on the angular resolution allows us to maintain consistency with previous works (e.g., D. S. Hudson et al. 2010; S. L. Hamer et al. 2012; T. Pasini et al. 2019, 2021; L. Rosignoli et al. 2024); and (3) adopting the broader statistical regions as uncertainties would not alter our conclusions of Section 4.1 and 4.3, that the position of the X-ray peak has a limited effect on the activation of the SMBH and rather supports it.

We point out that while our analysis was performed on broadband (0.5–7 keV) Chandra images (as in D. S. Hudson et al. 2010), previous observational and numerical studies point to a stronger correlation between warm ionized gas (traced by Hα) and soft ($\lesssim$1 keV) X-rays (e.g., A. C. Fabian et al. 2006; Y. Li & G. L. Bryan 2014). To evaluate this possibility, we repeated the analysis using soft-band Chandra images, limited to the 0.5–1.2 keV band. From these, we identified the soft-X-ray peak and compared it with that obtained from the broadband images. The results are presented in Figure 5. We find that the soft-X-ray peak position (pink triangle) is generally very similar to that derived from the broadband image (red square), and the corresponding confidence regions (pink and red dashed contours) are nearly identical. The only noticeable difference occurs in A3581, where the soft-X-ray peak is offset slightly farther from the SMBH compared to the broadband peak, though it still falls within the same confidence region. For these reasons, we restrict the analysis to the results obtained from the broadband X-ray images.

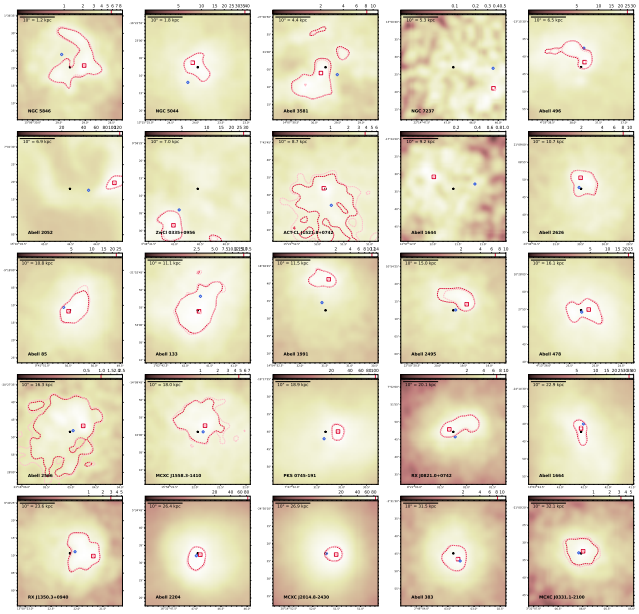

Figure 5. The same as Figure 6 but without the Hα contours. The red square and pink triangle mark the positions of the X-ray peaks in the broadband (0.5–7 keV) and soft-band (0.5–1.2 keV) X-ray images, respectively (see Appendix B.3 for details). The dashed red and pink contours outline "statistical confidence regions" for the positions of the X-ray peaks (in the broadband and soft-band X-ray images, respectively), defined as the area containing pixels with X-ray counts $N_C > N_C^P - \sqrt{N_C^P}$, where N_C^P is the number of counts in the pixel corresponding to the X-ray peak. The vertical red line on the color bar indicates the count level that defines this contour (for the broadband). The black star marks the SMBH position (see Table 1). No contours are shown for ACT-CL J1521.8+0742 and A1644, as their X-ray surface brightness is below 1 count per pixel. In these cases, the statistical confidence region for the brightest pixel would formally extend to the edge of the Chandra image. As noted in Appendix B.3, these contours would represent the confidence regions for the positions of the X-ray peaks in terms of X-ray counts, but we consider in our results the more conservative astrometric uncertainty of the X-ray data. We also show the location of the centroid of the X-ray surface brightness distribution with a blue diamond (see Appendix B.3 for details).

Ultimately, we investigate how the X-ray peak position compares with the center of the potential well of the host group or cluster, taken as the centroid of the X-ray surface brightness distribution (e.g., G. Gozaliasl et al. 2019). As shown in Figure 5, the X-ray centroid (blue diamond) is usually not coincident with the X-ray peak, although they are always at $\leqslant$10 kpc from each other. Relative to the X-ray peak, the centroid lies closer to the SMBH in $11/25$ systems, at a similar distance in $8/25$ systems, and farther away in $6/25$ systems. This suggests that the center of the potential well (the centroid) correlates slightly better than the density peak (the X-ray peak) with the SMBH position. We note, however, that in several cases where the centroid is formally closer to the SMBH than the X-ray peak, it does not coincide with the brightest X-ray emission region (e.g., A2052, ZwCl 0335+096, A1991, A2495, and A2566; see Figure 5). This is consistent with the centroid tracing the long-term center of the potential well rather than the present location of the cooling peak.

Appendix C
Multiwavelength Figures

We show multiwavelength views of the systems in our selection in Figure 6, where we overlay MUSE Hα contours on top of the Chandra X-ray image and show the VLBA image (for the detections) in a zoomed-in inset. In each main panel, we also report the positions of the components whose coordinates are shown in Table 1, using circles, squares, and stars.

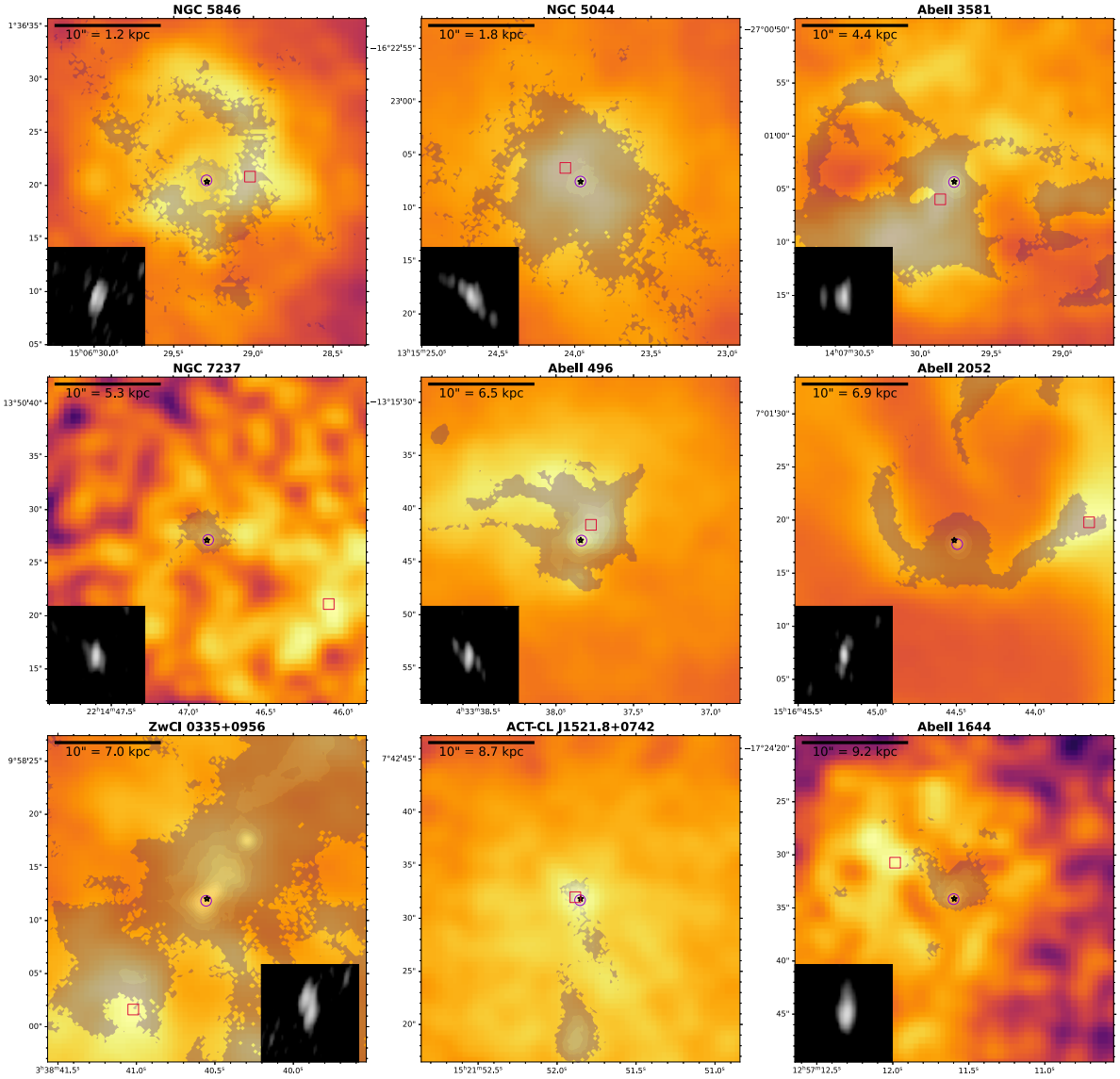

Figure 6. Multiwavelength views of the systems in our sample. The panels show smoothed X-ray Chandra maps of the hot gas, with grayscale contours of the Hα line from MUSE data. The red square marks the position of the X-ray peak, the purple circle shows the location of the Hα peak, and the black star shows the position of the SMBH (see Table 1). When detected, the VLBA image of the parsec-scale radio core is shown in the insets.

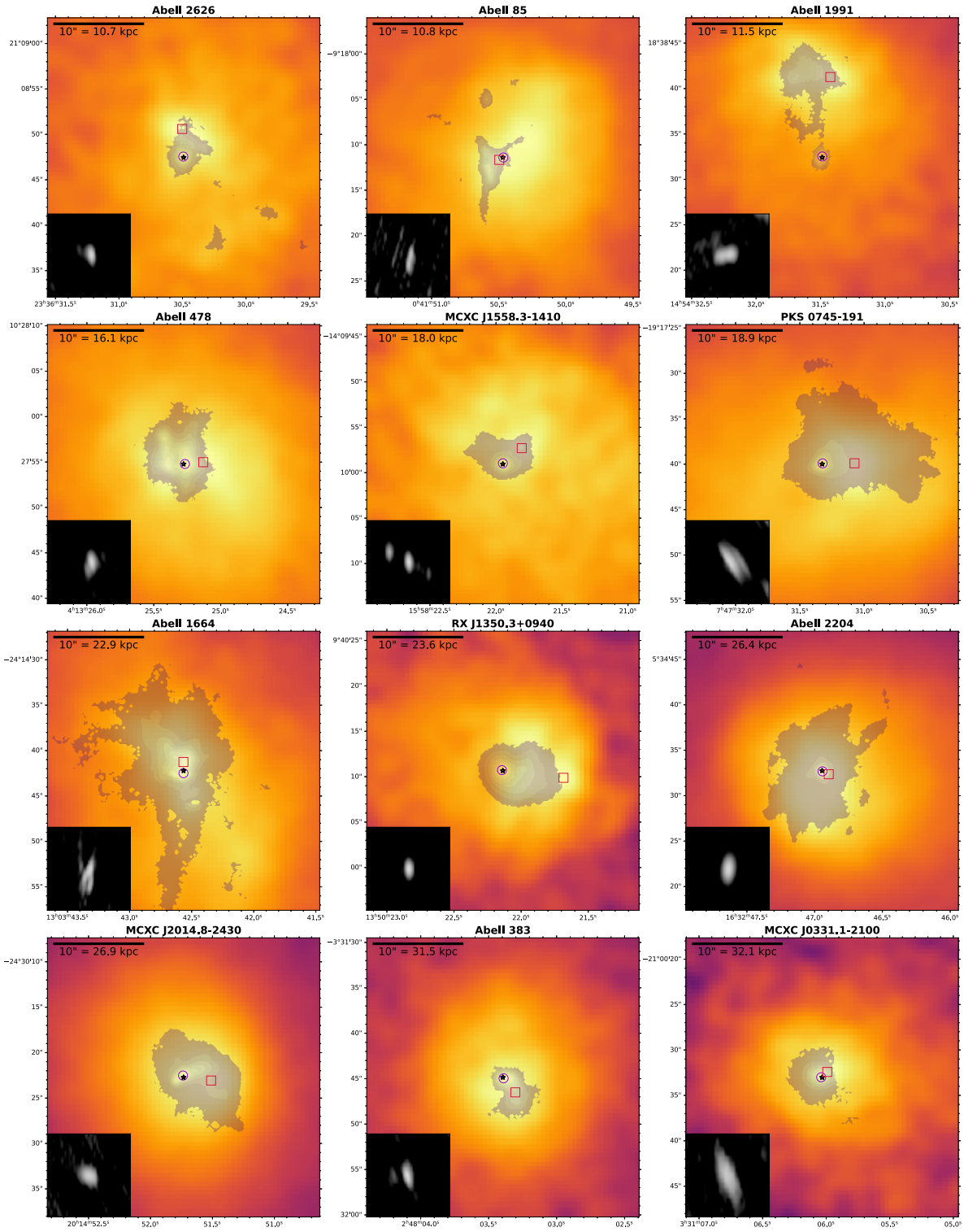

Figure 6. (Continued.)

Appendix D
BPT Diagrams

While the X-ray emissivity is mostly proportional to the gas density, $\epsilon_X \propto n_e^2 (kT)^{1/2}$, the H$\alpha$ luminosity is related both to the mass of the warm gas and to the ionizing flux. In this sense, a potential vicious circle for systems where the Hα peak lies on top of the radio AGN is represented by the possibility that the AGN itself is a dominant source of ionization. To verify this point, we made use of the wide wavelength range of MUSE and produced maps of the Hβ4861 Å, [O III]5007 Å, and [N II]6584 Å intensities, in addition to Hα, in order to use the well-known BPT diagram to separate between star formation, AGN photoionization, a LINER, and composite mechanisms as the dominant ionization source (J. A. Baldwin et al. 1981; L. J. Kewley et al. 2001, 2006; G. Kauffmann et al. 2003; R. Cid Fernandes et al. 2010). In producing these

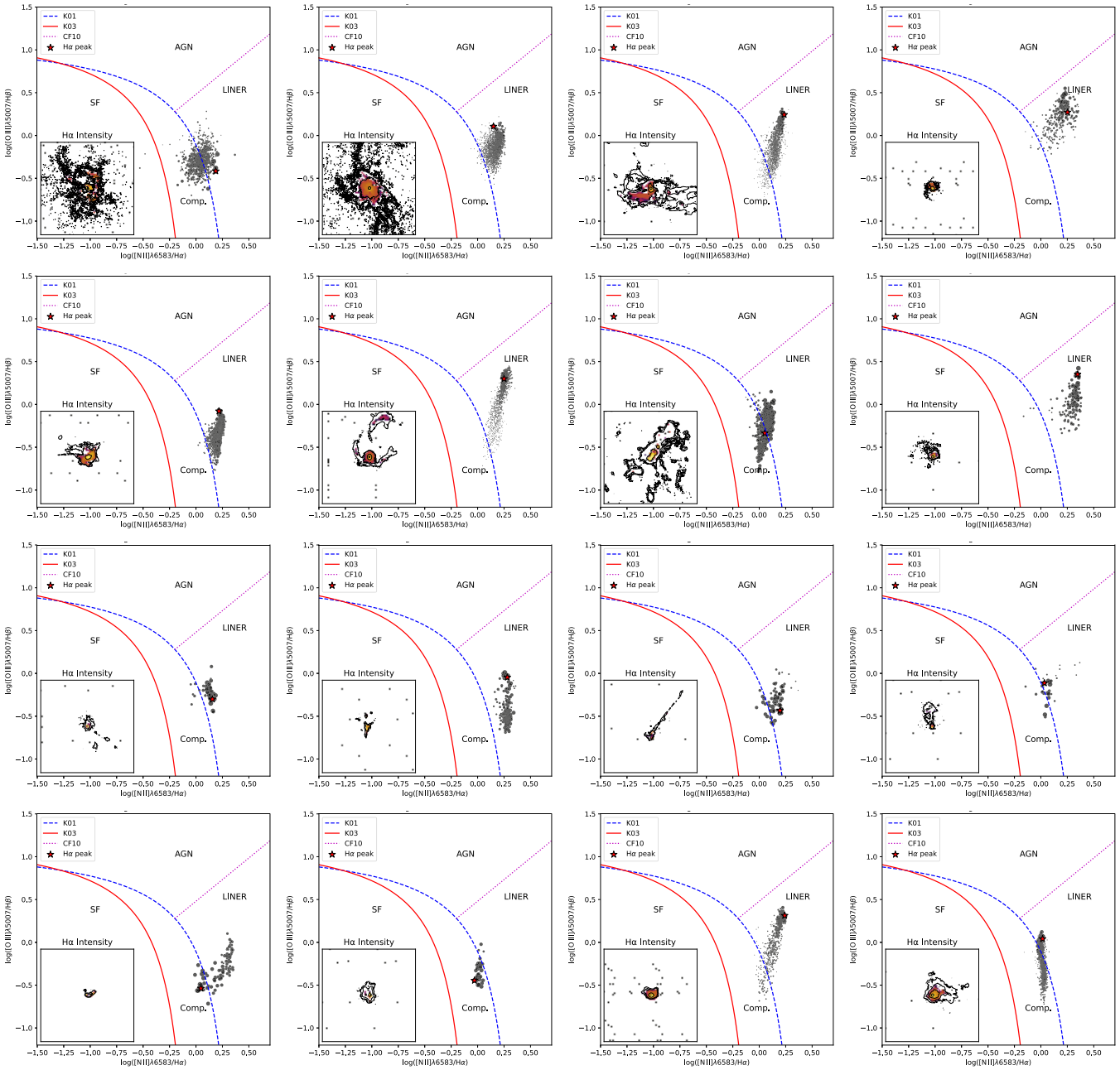

Figure 7. BPT diagram of the systems in our sample from MUSE data, showing the line ratio log([O III] $\lambda5007/\mathrm{H}\beta$) vs. log([N II] $\lambda6583/\mathrm{H}\alpha$) for spaxels with SNR >3 in all four lines. Systems that do not fulfill this requirement in any spaxel are marked. The standard demarcation curves from L. J. Kewley et al. (2001; K01), G. Kauffmann et al. (2003; K03), and R. Cid Fernandes et al. (2010; CF10) are overlaid to distinguish between regions dominated by star formation, AGN photoionization, composite activity, and LINER-like excitation. The position of the Hα peak is highlighted with a red star. The sizes of the black points are proportional to their Hα intensity. The subplot to the left shows the Hα intensity (black contours) and the subset of spaxels with SNR >3 in all four lines (colors). The absence of points in the AGN region confirms that the warm-gas emission is not dominated by AGN photoionization, supporting the interpretation of a non-AGN origin for the ionization near the Hα peak. From left to right, top to bottom: NGC 5846, NGC 5044, A3581, NGC 7237, A496, A2052, ZwCl 0335+096, A1644, A2626, A85, A133, A1991, A2495, A478, MCXC J1558.3-1410, PKS 0745-191, RXJ 0821.0+0752, A1664, RXJ 1350.3+0940, MCXC J2014.8-2430, A383, and MCXC J0331.1-2100.

maps, we considered only the pixels with SNRs greater than 3 in all the four lines (e.g., B. M. Poggianti et al. 2019). We can thus assess the ionization source only for a fraction of the whole Hα nebula. However, this is not an issue, since we are interested in the peak that typically has the highest SNR. For three systems (ACT-CL J1521.8+0742, A2566, and A2204), no spaxels met the SNR >3 threshold in all four lines—primarily due to the weakness of [O III]5007 Å—so BPT plots are not shown for these cases. We stress here that a detailed analysis of the BPT diagrams (such as the spatial variation in metallicity or density across the nebula) is outside the scope of this paper. Instead, we focus on the relative positions of the Hα peak and the surrounding nebula within the BPT plots.

Based on our inspection of the BPT diagrams (Figure 7), we find that none of the spaxels with SNR >3 lie in the AGN photoionization region. The warm gas of the systems in our sample is predominantly ionized by star formation or LINER-like processes (e.g., shocks), as previously found in other

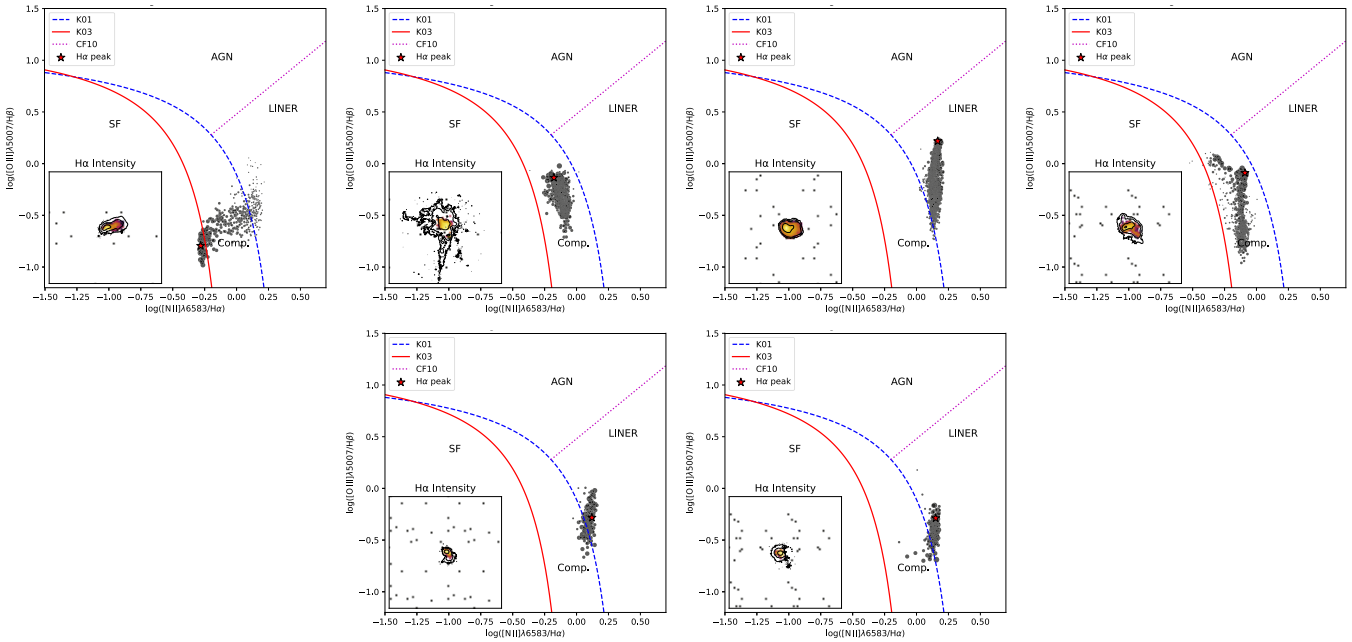

Figure 7. (Continued.)

works (K. Fogarty et al. 2015; S. L. Hamer et al. 2016; F. L. Polles et al. 2021). Moreover, there are no significant differences between the ionization conditions at the Hα peak and those across the surrounding warm gas, suggesting that the warm gas near the peak shares the same ionization mechanisms as the extended filamentary structure. This indicates that our analysis is not flawed by AGN photoionization producing a peak exactly where the AGN lies. We note that additional analysis using alternative BPT diagrams based on different line ratios ([O I]6300 Å/Hα and [S II]6717,6731 Å/Hα—not shown here; e.g., B. M. Poggianti et al. 2019) yielded consistent results.

ORCID iDs

Francesco Ubertosi https://orcid.org/0000-0001-5338-4472
Fabrizio Brighenti https://orcid.org/0000-0001-9807-8479
Ewan O'Sullivan https://orcid.org/0000-0002-5671-6900
Gerrit Schellenberger https://orcid.org/0000-0002-4962-0740
Myriam Gitti https://orcid.org/0000-0002-0843-3009
Simona Giacintucci https://orcid.org/0000-0002-1634-9886
Pasquale Temi https://orcid.org/0000-0002-8341-342X
Laurence P. David https://orcid.org/0009-0003-9413-6901
Jan Vrtilek https://orcid.org/0009-0007-0318-2814
Tiziana Venturi https://orcid.org/0000-0002-8476-6307
Elisabetta Liuzzo https://orcid.org/0000-0003-0995-5201
Marcella Massardi https://orcid.org/0000-0002-0375-8330
Kamlesh Rajpurohit https://orcid.org/0000-0001-7509-2972

References

Allen, S. W., Dunn, R. J. H., Fabian, A. C., Taylor, G. B., & Reynolds, C. S. 2006, MNRAS, 372, 21
Ascasibar, Y., & Markevitch, M. 2006, ApJ, 650, 102
Baldwin, J. A., Phillips, M. M., & Terlevich, R. 1981, PASP, 93, 5
Bambic, C. J., Russell, H. R., Reynolds, C. S., et al. 2023, MNRAS, 522, 4374
Bayer-Kim, C. M., Crawford, C. S., Allen, S. W., Edge, A. C., & Fabian, A. C. 2002, MNRAS, 337, 938
Bondi, H. 1952, MNRAS, 112, 195
Briggs, D. S. 1995, PhD thesis, New Mexico Institute of Mining and Technology
Cavagnolo, K. W., Donahue, M., Voit, G. M., & Sun, M. 2009, ApJS, 182, 12
Cheng, X., An, T., Baan, W. A., et al. 2025, ApJS, 277, 56
Cid Fernandes, R., Stasińska, G., Schlickmann, M. S., et al. 2010, MNRAS, 403, 1036
Condon, J. J., Cotton, W. D., & Broderick, J. J. 2002, AJ, 124, 675
Cui, W., Power, C., Biffi, V., et al. 2016, MNRAS, 456, 2566
Dallacasa, D., Orienti, M., Fanti, C., & Fanti, R. 2021, MNRAS, 504, 2312
Doi, A., Nakanishi, K., Nagai, H., Kohno, K., & Kameno, S. 2011, AJ, 142, 167
Donahue, M., & Voit, G. M. 2004, in Clusters of Galaxies: Probes of Cosmological Structure and Galaxy Evolution, ed. J. S. Mulchaey, A. Dressler, & A. Oemler (Cambridge: Cambridge Univ. Press), 143
Donahue, M., & Voit, G. M. 2022, PhR, 973, 1
Eckert, D., Gaspari, M., Gastaldello, F., Le Brun, A. M. C., & O'Sullivan, E. 2021, Univ, 7, 142
Edge, A. C. 2001, MNRAS, 328, 762
European Southern Observatory (ESO) 2016, European Southern Observatory (ESO),
Fabian, A. C. 2012, ARA&A, 50, 455
Fabian, A. C., Sanders, J. S., Taylor, G. B., et al. 2006, MNRAS, 366, 417
Fogarty, K., Postman, M., Connor, T., Donahue, M., & Moustakas, J. 2015, ApJ, 813, 117
Fruscione, A., McDowell, J. C., Allen, G. E., et al. 2006, Proc. SPIE, 6270, 62701V
Fujita, Y., Kawakatu, N., & Shlosman, I. 2016, PASJ, 68, 26
Gaspari, M., Ruszkowski, M., & Oh, S. P. 2013, MNRAS, 432, 3401
Gaspari, M., Temi, P., & Brighenti, F. 2017, MNRAS, 466, 677
Gaspari, M., Tombesi, F., & Cappi, M. 2020, NatAs, 4, 10
Gitti, M., Brighenti, F., & McNamara, B. R. 2012, AdAst, 2012, 950641
Gitti, M., Nulsen, P. E. J., David, L. P., McNamara, B. R., & Wise, M. W. 2011, ApJ, 732, 13
Gozaliasl, G., Finoguenov, A., Tanaka, M., et al. 2019, MNRAS, 483, 3545
Graham, A. W. 2007, MNRAS, 379, 711
Greisen, E. W. 1990, in Acquisition, Processing and Archiving of Astronomical Images, ed. G. Longo & G. Sedmak (Napoli: Osservatorio Astronomico di Capodimonte), 125
Greisen, E. W. 2003, in Information Handling in Astronomy—Historical Vistas, ed. A. Heck (Dordrecht: Springer), 109
Hamer, S. L., Edge, A. C., Swinbank, A. M., et al. 2012, MNRAS, 421, 3409
Hamer, S. L., Edge, A. C., Swinbank, A. M., et al. 2016, MNRAS, 460, 1758
Hatch, N. A., Crawford, C. S., Johnstone, R. M., & Fabian, A. C. 2006, MNRAS, 367, 433
Hogan, M. T., Edge, A. C., Geach, J. E., et al. 2015a, MNRAS, 453, 1223
Hogan, M. T., Edge, A. C., Hlavacek-Larrondo, J., et al. 2015b, MNRAS, 453, 1201
Hudson, D. S., Mittal, R., Reiprich, T. H., et al. 2010, A&A, 513, A37

Johnson, R. E., Zuhone, J., Jones, C., Forman, W. R., & Markevitch, M. 2012, ApJ, 751, 95
Kadam, S. K., Sonkamble, S. S., Vagshette, N. D., & Patil, M. K. 2024, NewA, 111, 102253
Kauffmann, G., Heckman, T. M., Tremonti, C., et al. 2003, MNRAS, 346, 1055
Kewley, L. J., Dopita, M. A., Sutherland, R. S., Heisler, C. A., & Trevena, J. 2001, ApJ, 556, 121
Kewley, L. J., Groves, B., Kauffmann, G., & Heckman, T. 2006, MNRAS, 372, 961
Kirkpatrick, C. C., & McNamara, B. R. 2015, MNRAS, 452, 4361
Li, Y., & Bryan, G. L. 2014, ApJ, 789, 54
Liuzzo, E., Taylor, G. B., Giovannini, G., & Giroletti, M. 2009, A&A, 501, 933
Longair, M. S. 2011, High Energy Astrophysics (Cambridge: Cambridge Univ. Press)
Markevitch, M., & Vikhlinin, A. 2007, PhR, 443, 1
Mathews, W. G., & Brighenti, F. 2003, ARA&A, 41, 191
McDonald, M., Veilleux, S., Rupke, D. S. N., & Mushotzky, R. 2010, ApJ, 721, 1262
McMullin, J. P., Waters, B., Schiebel, D., Young, W., & Golap, K. 2007, in ASP Conf. Ser. 376, Astronomical Data Analysis Software and Systems XVI, ed. R. A. Shaw, F. Hill, & D. J. Bell (San Francisco, CA: ASP), 127, https://www.aspbooks.org/a/volumes/article_details/?paper_id=5267
McNamara, B. R., & Nulsen, P. E. J. 2007, ARA&A, 45, 117
McNamara, B. R., & Nulsen, P. E. J. 2012, NJPh, 14, 055023
McNamara, B. R., Russell, H. R., Nulsen, P. E. J., et al. 2016, ApJ, 830, 79
Middelberg, E., Deller, A. T., Norris, R. P., et al. 2013, A&A, 551, A97
Million, E. T., Allen, S. W., Werner, N., & Taylor, G. B. 2010, MNRAS, 405, 1624
Olivares, V., Picquenot, A., Su, Y., et al. 2025, NatAs, 9, 449
Olivares, V., Salome, P., Combes, F., et al. 2019, A&A, 631, A22
Olivares, V., Salomé, P., Hamer, S. L., et al. 2022, A&A, 666, A94
Panessa, F., Baldi, R. D., Laor, A., et al. 2019, NatAs, 3, 387
Pasini, T., Gitti, M., Brighenti, F., et al. 2019, ApJ, 885, 111
Pasini, T., Gitti, M., Brighenti, F., et al. 2021, ApJ, 911, 66
Pizzolato, F., & Soker, N. 2005, ApJ, 632, 821
Poggianti, B. M., Gullieuszik, M., Tonnesen, S., et al. 2019, MNRAS, 482, 4466
Polles, F. L., Salomé, P., Guillard, P., et al. 2021, A&A, 651, A13
Prasad, D., Voit, G. M., & O'Shea, B. W. 2024, MNRAS, 531, 259
Pulido, F. A., McNamara, B. R., Edge, A. C., et al. 2018, ApJ, 853, 177
Randall, S. W., Clarke, T. E., Nulsen, P. E. J., et al. 2010, ApJ, 722, 825
Reynolds, C. S., Kara, E. A., Mushotzky, R. F., et al. 2023, Proc. SPIE, 12678, 126781E
Rosignoli, L., Ubertosi, F., Gitti, M., et al. 2024, ApJ, 963, 8
Russell, H. R., McNamara, B. R., Edge, A. C., et al. 2013, MNRAS, 432, 530
Russell, H. R., McNamara, B. R., Fabian, A. C., et al. 2019, MNRAS, 490, 3025
Sanderson, A. J. R., O'Sullivan, E., & Ponman, T. J. 2009, MNRAS, 395, 764
Schellenberger, G., O'Sullivan, E., David, L. P., et al. 2024, ApJ, 976, 246
Sokolovsky, K. V., Kovalev, Y. Y., Pushkarev, A. B., & Lobanov, A. P. 2011, A&A, 532, A38
Su, Y., Nulsen, P. E. J., Kraft, R. P., et al. 2017, ApJ, 851, 69
Tremonti, C. A., Heckman, T. M., Kauffmann, G., et al. 2004, ApJ, 613, 898
Ueda, S., Ichinohe, Y., Molnar, S. M., Umetsu, K., & Kitayama, T. 2020, ApJ, 892, 100
van den Bosch, F. C., Weinmann, S. M., Yang, X., et al. 2005, MNRAS, 361, 1203
Vantyghem, A. N., McNamara, B. R., Russell, H. R., et al. 2019, ApJ, 870, 57
Voit, G. M., Meece, G., Li, Y., et al. 2017, ApJ, 845, 80
Weilbacher, P. M., Streicher, O., Urrutia, T., et al. 2014, in ASP Conf. Ser. 485, Astronomical Data Analysis Software and Systems XXIII, ed. N. Manset & P. Forshay (San Francisco, CA: ASP), 451, https://www.aspbooks.org/publications/485/451.pdf
Werner, N., Simionescu, A., Million, E. T., et al. 2010, MNRAS, 407, 2063
Wu, Q., & Cao, X. 2005, ApJ, 621, 130
Xu, C., Baum, S. A., O'Dea, C. P., Wrobel, J. M., & Condon, J. J. 2000, AJ, 120, 2950
Zuhone, J. A., & Roediger, E. 2016, JPlPh, 82, 535820301